# Challenges in Seafloor Imaging and Mapping With Synthetic Aperture Sonar

Roy Edgar Hansen, *Member, IEEE*, Hayden John Callow, *Member, IEEE*, Torstein Olsmo Sæbø, *Member, IEEE*, and Stig Asle Vaksvik Synnes

*Abstract*—Synthetic aperture sonar (SAS) is emerging as an imaging technology that can provide centimeter resolution over hundreds of metres range on the seafloor. Although the principle of SAS has been known for more than 30 years, SAS systems have only recently become commercially available. The success of SAS is critically dependent on overcoming several challenges related to the ocean environment. The sonar has to be positioned with accuracy better than a fraction of a wavelength along the synthetic aperture. We use the sensor itself for navigation in combination with aided inertial navigation. The sound velocity has to be accurately estimated for successful focusing of SAS images. We calculate a simple rule-of-thumb for tolerance and show the effect of incorrect sound velocity. For non-straight synthetic apertures, the bathymetry must be estimated. We use real aperture interferometry to map the scene before SAS processing. We calculate the required bathymetry accuracy and show effects of insufficient mapping. Vehicle instability and non-straight tracks in combination with insufficient navigation accuracy can cause grating lobes in the SAS images, not common in single-channel SAR. We show example imagery with severe grating lobes. In shallow waters, the acoustic signals will interact with the sea surface, possibly causing multipath. This will reduce the SAS quality. We use coherence to map the signal to multipath and thereby the valid sensor range. This paper illustrates the different challenges using examples from the HISAS 1030 interferometric SAS.

*Index Terms*—Synthetic aperture sonar, synthetic aperture radar, interferometry, seafloor imaging, navigation, sound velocity errors, topography errors, non-linear tracks, multiple reflections

## I. INTRODUCTION

SYNTHETIC aperture sonar (SAS) is less known and developed than its counterpart in radar. Although the principle of SAS is not new [1], [2], it is only during latest years that SAS systems have become commercially available. The Norwegian Defence Research Establishment (FFI) and Kongsberg Maritime have a long term collaboration to develop SAS for the HUGIN autonomous underwater vehicle (AUV) [3]. Fig. 1 shows a HUGIN 1000-MR AUV with the HISAS 1030 interferometric SAS onboard a Royal Norwegian Navy mine hunter.

There are a few critical differences between SAR and SAS [4], particularly related to the environment for which the sensor is operating. This paper describes some of the specific
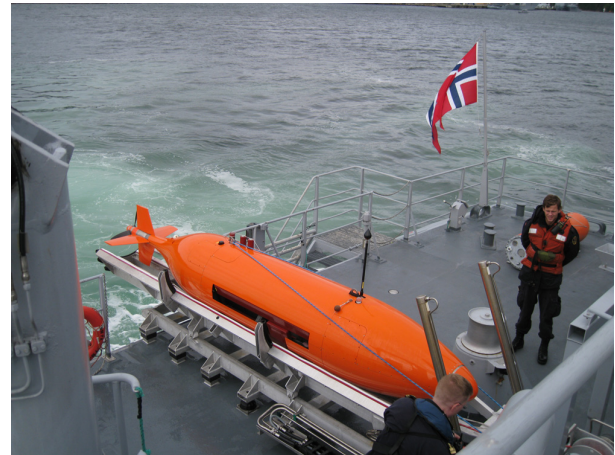
Fig. 1. HUGIN 1000-MR AUV equipped with the HISAS 1030 interferometric SAS onboard the Royal Norwegian Navy mine hunter Hinnøy.

challenges in SAS and how we approach them in imaging and mapping of the seafloor from autonomous underwater vehicles.

The sonar has to be positioned with accuracy better than a fraction of a wavelength along the synthetic aperture. This is non-trivial under water where GPS is not available. One solution is using the sensor itself for navigation in combination with aided inertial navigation. The ocean environment, and in particular, the sound velocity, has to be accurately estimated for successful focusing of SAS images. The sound velocity can change up to 2% over a typical depth profile. SAS is nearfield imaging, and an error of 0.2% in sound velocity can cause defocus. For non-straight synthetic apertures, the bathymetry of the scene to be imaged must be known. This is a significant problem in SAS since the range of the system is relatively short compared to topography changes in heavy terrain. Because of the relatively low sound speed (which limits the maximum pulse repetition frequency), almost all existing practical SAS systems today are multi-element receiver systems. Vehicle instability and non-straight tracks combined with insufficient navigation accuracy can cause periodic errors in the synthetic aperture and grating lobes in the SAS images, not common in single-channel SAR. In shallow waters, the acoustic signals will interact with the sea surface, possibly causing multipath. This will reduce the SAS image quality.

In Section II we describe the sensor and the signal processing we have developed for the HISAS 1030 interferometric SAS. Section III describes the main differences between SAS and SAR. The specific challenges in SAS are described in

Fig. 2. The HISAS 1030 interferometric SAS mounted on a HUGIN 1000-MR autonomous underwater vehicle.



Fig. 3. SAS signal processing overview for full swath stripmap SAS.

Section IV. Finally, we conclude in Section V.

## II. SYSTEM DESCRIPTION

### A. Sensor

HISAS 1030 is a wideband widebeam interferometric SAS developed by Kongsberg Maritime and FFI [5], [6]. The sonar contains two along-track receiver arrays of 1.2 m length with 32 elements in each array, and a vertical baseline approximately 30 cm which equals 20 wavelengths. The transmitter is a vertical phased array with 16 elements, and the transmit beam can be electronically steered and shaped to obtain the best possible performance in shallow waters (see Section IV-E). The transmitter can also be used as a receiver, giving 16 individual receiver channels along a vertical array. Fig. 2 shows the sonar mounted on a HUGIN 1000-MR AUV. Typical HISAS 1030 specifications are approximated in Table I.

### B. Signal processing

The signal processing of SAS data is similar to any SAR processor, with a few exceptions. FFI has developed a software package named *FOCUS Toolbox* for all signal processing of the SAS data [7]. Fig. 3 shows an overview of the processing flow. We use all relevant data about the environment, the topography and the navigation to obtain the best possible results. We use the sonar data for navigation before SAS imaging (see Section IV-A). We also use real aperture interferometry (or sidescan bathymetry) [8] to map the area before imaging (see Section IV-C). The blocking algorithm divides the collected

TABLE I
TYPICAL SYSTEM SPECIFICATIONS FOR THE HISAS 1030
INTERFEROMETRIC SAS.

| Center frequency | 100 kHz |
|---|---|
| Wavelength | 1.5 cm |
| Bandwidth | 30 kHz |
| Total frequency range | 50-120 kHz |
| Along-track resolution | 3 cm |
| Cross-track resolution | 3 cm |
| Maximum range @ 2 m/s | 200 m |
| Area coverage rate | 2 km$^2$/h |

data into suitable blocks of data to be processed [9]. We use the wavenumber algorithm [10], [11, chapter 8] (also referred to as range migration algorithm or Omega-K algorithm) for full swath large scale imaging. HISAS 1030 has large relative bandwidth and large beamwidth. We have therefore not used the chirp scaling algorithm [11, chapter 7], [12]. The motion compensation is either wide beam or narrow beam, dependent on the actual tracks [13, chapter 6]. We then do interferometric processing for full swath bathymetry (if required) [14], [15].

When searching for small objects of interest, a second processing stage is applied [16], as illustrated in Fig. 4. This enables the possibility to apply enhancement of images as part of the target recognition. In the second stage, we can reprocess small areas of interest in higher resolution and/or using better navigation solutions. We use the backprojection algorithm [17, pages 117-119] (or delay-and-sum) in three dimensions for this. Possible enhancements are target enhancement using autofocus [18, chapter 4], [13]; shadow enhancement using fixed focusing [19], [20]; multi-aspect imagery [16]; and SAS interferometry in high resolution [15].

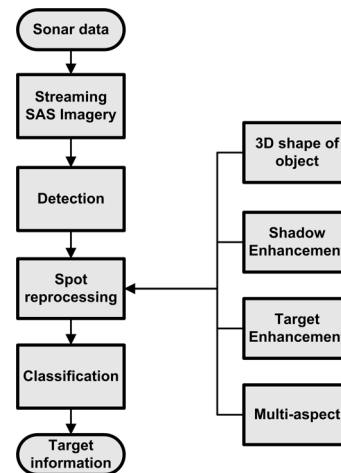Fig. 5 shows an example image that captures the essence



Fig. 4. Two stage SAS processing to facilitate image enhancement for target recognition. Spot reprocessing is not to be confused with spotlight synthetic aperture processing.
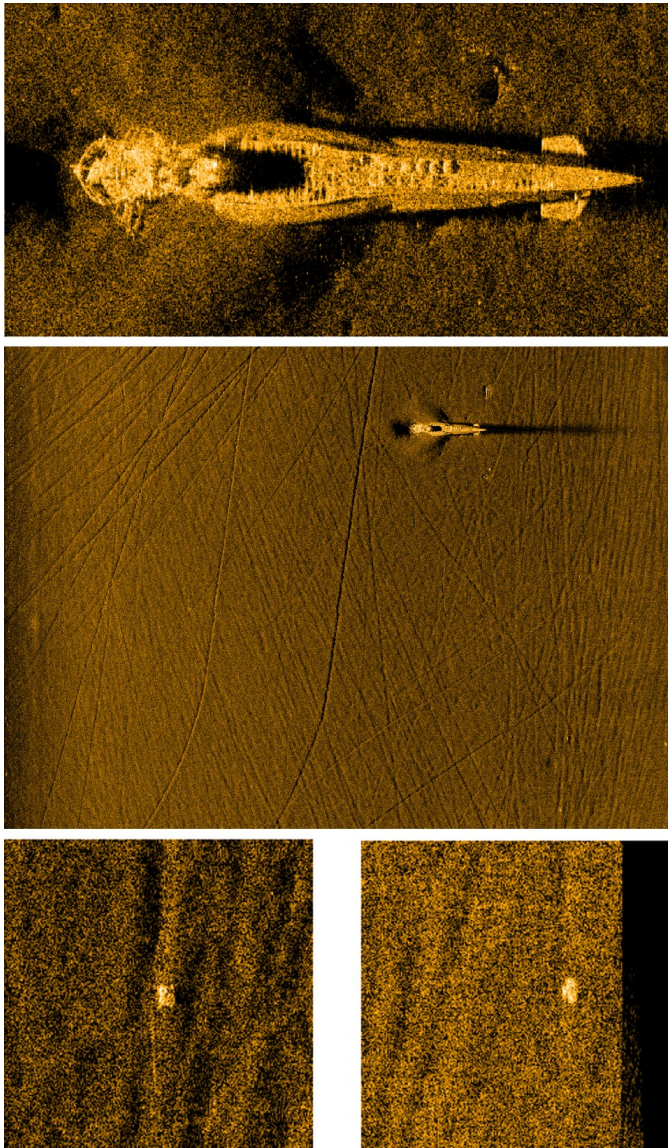
Fig. 5. Example imagery that illustrates the performance of HISAS 1030. The range in the center panel is 25–325 m (left to right) and the water depth 180–200 m. Top inset: A $40 \times 20$ m cutout around the wreck of the German WWII submarine U-735, centred at 225 m range. Bottom insets: Cutout around $1 \times 1$ m concrete cubes, centred at 275 m range (left) and 320 m range (right). Theoretical resolution in the image is $3 \times 3$ cm.

of SAS and illustrates the performance of HISAS 1030. The SAS resolution-gain, defined as the ratio between along-track resolution in real aperture $\delta x_{RA}$ and synthetic aperture $\delta x_{SA}$ is [21, pages 25-28]

$$Q_{SA} = \frac{\delta x_{RA}}{\delta x_{SA}} \approx R \frac{\lambda}{L} \frac{2}{d}, \qquad (1)$$

where $R$ is the range, $\lambda$ is the wavelength at center frequency, $d$ is the along-track element size in the array and $L$ is the array length. In Fig. 5, the SAS resolution-gain is $Q_{SA} \approx 200$ at maximum range. This is a considerable resolution improvement, and the equivalent along-track resolution is very difficult to obtain using real aperture techniques.

## TABLE II
APPROXIMATE RANGE $R$ FOR FREQUENCY $f$ AND CORRESPONDING WAVELENGTH $\lambda$.

| $f$ [kHz] | $R$ [km] | $\lambda$ [m] |
|---|---|---|
| 0.1 | 1000 | 15 |
| 1 | 100 | 1.5 |
| 10 | 10 | 0.15 |
| 100 | 1 | 0.015 |
| 1000 | 0.1 | 0.0015 |

## III. DIFFERENCES BETWEEN SAR AND SAS

The principle for synthetic aperture imaging is the same in radar and sonar. There are, however, some rather important differences between SAR and SAS. These differences are related to the ocean environment and the differences in phase velocity.

### A. Frequency

Seawater is a dissipative medium through viscosity and chemical processes [22, pages 9-11], [23, pages 19-23], [24, pages 104-110]. Acoustic absorption in seawater is frequency dependent, so lower frequencies reach longer than higher frequencies. The frequency relation to absorption is such that the traveling distance measured in wavelengths more or less has a fixed absorption loss. The one way achievable range (for a 150 dB transmission loss) is summarized in Table II. This gives an upper limit on the frequency for any given range. This will, inherently, limit the along-track resolution for real aperture sonars, such as sidescan sonar and multibeam echo sounders [23, chapter 8].

### B. Along-track sampling

The most significant difference between SAR and SAS is the phase velocity, which typically is $c_r = 3 \times 10^8$ m/s for radio waves in air, and $c_a = 1.5 \times 10^3$ m/s for acoustic waves in seawater [22, pages 1-9], [23, pages 36-41]. The low phase velocity causes a fundamental problem in obeying the sampling criterion along the synthetic array. Using a multi-element receiver array is a technique to reduce this problem [1], [25], and almost all existing SAS systems today are multi-element receivers. The distance traveled between pulses can maximally be half the length of the receiver array [25], [26]. This gives a maximum range of

$$R_{max} = \frac{cL}{4\alpha v}, \qquad (2)$$

where $c$ is the sound velocity, $v$ is the vehicle speed, and $\alpha$ is an overlap factor $\geq 1$ controlling the relative redundancy in the synthetic aperture [27]. This redundancy can be used for micronavigation (see Section IV-A). The HISAS 1030 has $L = 1.2$ m giving a maximum range of $R_{max} = 203$ m at typical vehicle speed $v = 2$ m/s and overlap factor $\alpha = 32/29$.

### C. Imaging geometry

A typical AUV-based SAS imaging geometry is illustrated in Fig. 6. Two sonars are mounted on the vehicle, one on port side and one on starboard. The vehicle runs rather low over the
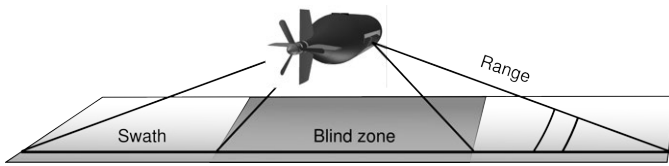
Fig. 6. Typical AUV based SAS imaging geometry for a twosided system. The port and starboard sonars have a very horizontal geometry, giving a blind zone underneath the vehicle.



Fig. 8. Basic geometry of synthetic aperture imaging in two dimensions.

seafloor, and the sonar range is typically 10 times the vehicle altitude. Hence, the stand-off range is very small, only 1/10 of the swath width. Beneath the vehicle, there is a blind zone or a gap with a width approximately two times the altitude. The imaging geometry is thereby rather horizontal with reception of data from $45°$ to $5°$ grazing angle. A typical SAS system works in strip-map mode, with the swath width almost equal to the maximum range. In SAS, shadowing is a more dominant effect than foreshortening and layover compared to satellite borne SAR [21, chapter 1.5].

## IV. CHALLENGES IN SAS

The success of synthetic aperture sonar is critically dependent on overcoming several challenges [28], [29]. In this section, we list some of the important factors to consider to be able to perform robust and reliable SAS.

### A. Navigation

Navigation of autonomous underwater vehicles is more difficult than navigation of airborne and terrestrial platforms because GPS is not available. The HUGIN AUV is equipped with a high grade aided inertial navigation system (INS) [30]. Fig. 7 shows a schematic overview of the aided inertial system on the HUGIN AUV. The main components are the inertial measurement unit (IMU) and the Doppler Velocity Logger (DVL) in combination with an error state Kalman filter. Position updates can be provided but are not always available.

In synthetic aperture imaging, the sensor has to be positioned with accuracy better than a fraction of a wavelength
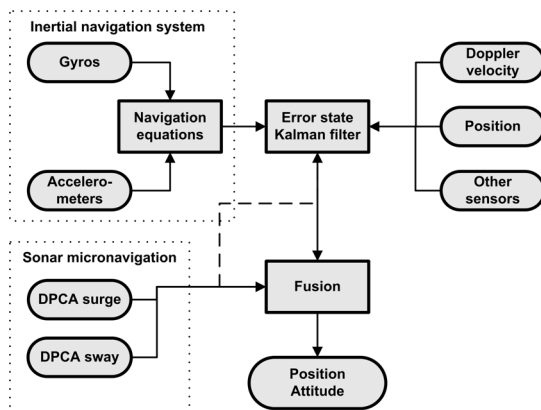


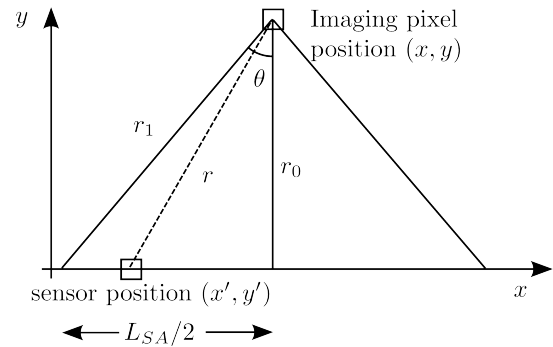Fig. 7. Navigation system on the HUGIN AUV with possible fusion with sonar micronavigation.

along the entire aperture. For a 100 kHz sonar in seawater, this equals an accuracy requirement around 1 millimetre along tens of metres of traveled distance. This requirement is generally not met even by the most advanced aided INS systems available for AUVs. One possible solution is to use the sonar itself as a navigation sensor (micronavigation) in combination with the inertial navigation system [31]. The micronavigation can be based on the principle of displaced phase centre antenna (DPCA) [27]. In radar, DPCA is mostly used for clutter suppression in ground moving target indication (GMTI) radar [32]. We use DPCA to estimate platform motion similar to shear averaging in SAR [33], [34]. The micronavigation estimates can either be fed into the error state Kalman filter for a tight integration, or fused outside the standard navigation solution. This is indicated with dashed lines in Fig. 7.

### B. Sound velocity errors

The sound velocity in the ocean varies with depth [22, pages 1-9], [23, pages 36-41]. There might also be local horizontal and temporal variations. This can cause variation in the sound velocity of up to 2% along the acoustic path.

SAS is near-field acoustic imaging. In this section, we describe the effect of an incorrect sound velocity in near field imaging. We will only consider the homogeneous case of constant sound velocity. Assume a two-dimensional imaging geometry for a monostatic system moving in a straight line along the $x$-axis, with range along the $y$-axis. This is illustrated in Fig. 8. In the single scattering approximation, the seafloor reflectivity function $\hat{f}(x, y)$ can be estimated by the *backprojection* algorithm [17, pages 117-119]

$$\hat{f}(x, y) = \int s(\tau, u)e^{-j2\pi f_c \tau} du, \qquad (3)$$

where $\tau = 2r/c$ is the two-way travel time, $s(\tau, u)$ the matched filtered (or pulse compressed) received signal for position $u$ along the synthetic aperture, $c$ the sound velocity and $f_c$ the carrier frequency. The two-way distance to the imaging pixel is

$$r = \sqrt{(x - x')^2 + (y - y')^2} = \sqrt{(x - u)^2 + y^2}, \qquad (4)$$

where $x'$ and $y'$ are the sonar positions. An incorrect sound velocity will cause an incorrect mapping between range and time. In the far field this will cause a shift in range of the

backprojected image, but no deformation. In the near field, the incorrect sound velocity will lead to relative errors in the geometry within the synthetic aperture, and thereby defocus. To characterize this effect, we calculate the *depth-of-focus* [35, pages 331-333], [36, page 108] parameterized as a function of the sound velocity error. Consider the synthetic aperture data collection for a particular pixel, as illustrated in Fig. 8. We define $r_0$ to be the minimum range (at broadside) and $r_1$ to be the maximum range which is obtained for sensor position at maximum observation angle (see Fig. 8). Assume a small range error $\delta r$ induced by incorrect sound velocity. The difference in range is

$$\varepsilon = (r_1' - r_1) - ((r_0 - \delta r) - r_0) \approx \delta r \frac{L_{SA}^2}{8r_0^2}, \quad (5)$$

where $L_{SA}$ is the length of the synthetic aperture. By choosing a maximum error of $\varepsilon = \lambda/8$ and setting $r_d = \delta r$, we get the *depth-of-focus*

$$r_d = \frac{\lambda r_0^2}{L_{SA}^2}. \quad (6)$$

A sound velocity error of $\delta c = c - c_0$ where $c$ is the true sound velocity and $c_0$ is the assumed (incorrect) sound velocity, will cause an approximate range error of

$$\delta r = \frac{\delta c}{c_0} r. \quad (7)$$

Inserting (7) in (6) for $r_d = \delta r$ and $r = r_0$, we get a simple rule for the tolerance for sound velocity error in SAS

$$\delta c \leq c_0 \frac{\lambda r_0}{L_{SA}^2}. \quad (8)$$

For a full length synthetic aperture, $L_{SA}$ is given by $r_0$ and the beamwidth $\beta = \lambda/d$, as

$$L_{SA} \approx r_0 \beta = r_0 \lambda/d, \quad (9)$$

where $d$ is the transmitter/receiver element size along-track. This gives the following rule of thumb for the tolerance

$$\delta c \leq \frac{c_0}{r_0} \frac{d^2}{\lambda}. \quad (10)$$

This is similar to the point scatter response spread given in [37]. A sound velocity error larger than the tolerance leads to defocusing and reduced image quality. Note that dependent on what the acceptable image quality loss is, there can be formed different requirements [38, page 210].

Fig. 9 shows the sound velocity error tolerance as function of range for three different frequencies. The results are shown for a sound velocity $c_0 = 1500$ m/s and equivalent element size of $d = 5$ cm. Interestingly, we see that the tolerance increases with frequency. This is due to a decrease in beamwidth for increasing frequency for fixed resolution (or element size).

Fig. 10 shows the sound velocity profile calculated from a conductivity, temperature, depth (CTD) profiler [39, vol. 1, pages 579-588] taken from a surface ship during a HUGIN mission outside Horten, Norway, in August 2006. The upper dashed line indicates the AUV depth during the SAS data collection, and the lower dashed line indicates the seafloor depth. The sound velocity varies with more than 20 m/s between the
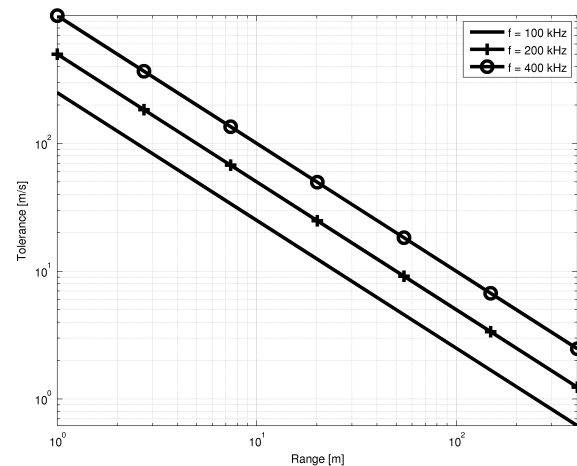


Fig. 9. Sound velocity error tolerance as function of range for three different frequencies with an equivalent element size of $d = 5$ cm. HISAS 1030 typically has 100 kHz center frequency.

vehicle and the seafloor. The vehicle also carries a high quality CTD sensor. By using this sensor (at vehicle depth) as input, the calculated sound velocity becomes too high, actually more than 10 m/s higher than the average sound velocity between vehicle and seafloor. According to the tolerance (10), the SAS image should defocus for any range larger than 30 m. Fig. 11 shows SAS images of two small scenes containing debris on the seafloor. The left pair is processed using the vehicle CTD (which is incorrect on average). The center pair of images is processed using the average sound velocity from vehicle depth to seafloor depth. These images are noticeably more focused and contain more detail. An incorrect sound velocity leads to a quadratic phase error, that can be estimated and corrected for by autofocusing [18, chapter 4]. We have applied a modified phase gradient autofocus (PGA) technique [40] to the image processed using vehicle CTD (left pair) with substantial defocusing. The right image pair shows the PGA
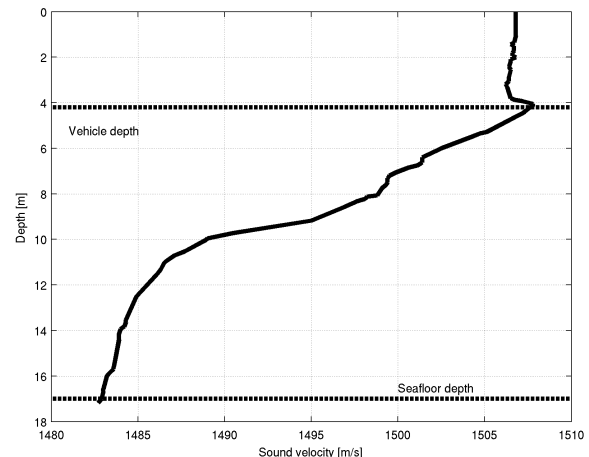


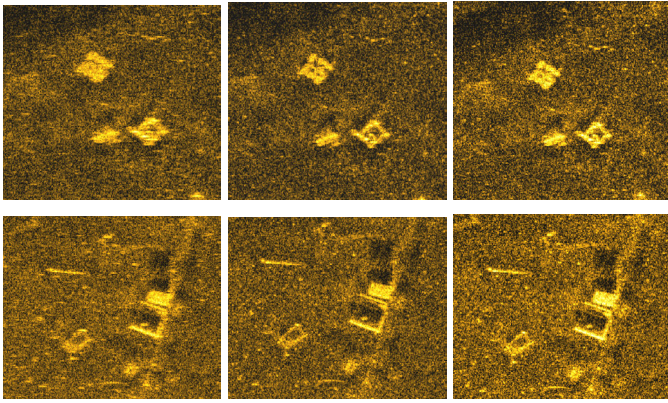Fig. 10. Sound velocity profile for a HUGIN mission in August 2006.

Fig. 11. SAS images of an area with debries on the seafloor. The area size is $5 \times 5$ m, and the range is 53 m for the lower row and 60 m for the upper row. Left: Using vehicle CTD for sound velocity. Middle: Using average sound velocity profile from vehicle depth to the seafloor. Right: Phase gradient autofocus of the vehicle CTD based images (left images).

corrected images. As Fig. 11 shows, PGA corrects for some of the defocusing, but it is better to use the average sound velocity.

In ocean environments with sound velocity gradients, refraction will occur [22, chapter 2], [23, chapter 2]. If not compensated for properly, this effect will also lead to defocusing [41]. We have found refraction effects to be less important than the average sound velocity error effect for the sharpness of the images. In bathymetric mapping with SAS interferometry, correction of refraction effects may be very important [42].

### C. Topographic errors

For non-straight synthetic apertures, the topography (or bathymetry) of the scene to be imaged has to be known [18, pages 187-197]. This is critical for robust AUV based SAS, and a significant problem since the range of the sonar is relatively short compared to the topographic changes in rough terrain [29]. Airborne SAR on small aircrafts or drones flying at low altitude have similar challenges [43]. The required
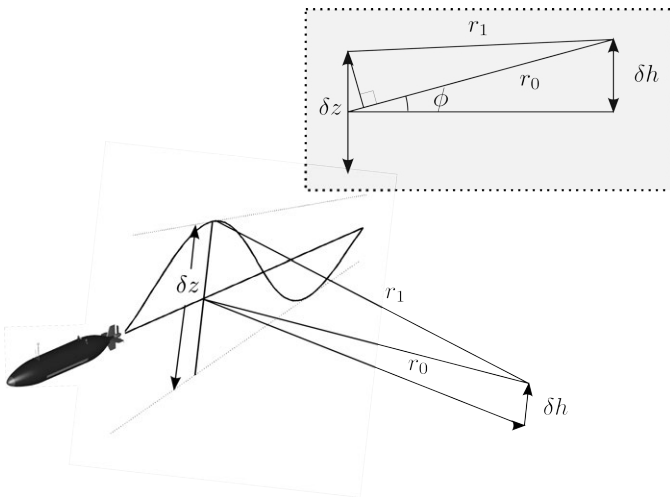


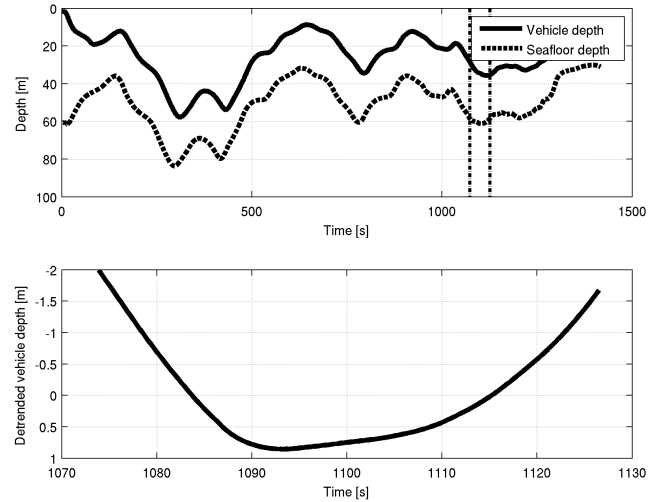Fig. 12. Motion deviation normal to the slant range direction.



Fig. 13. Top: Vehicle track and seafloor depth for a particular HISAS 1030 mission in Norwegian waters with rough terrain. Bottom: detrended vehicle depth from time interval 1073 s to 1127 s.

accuracy in the bathymetry can be calculated as follows. Assume a non-straight vehicle track with motion deviations of $\delta z$, as illustrated in Fig. 12. For an object placed a distance $\delta h$ orthogonal to the slant range plane, the imaging geometry becomes incorrect and defocus will occur. The difference in travel distance is

$$\delta r = 2(r_0 - r_1) \approx \delta z \sin \phi \approx \delta z \delta h / r_0, \tag{11}$$

where $\phi$ is the depression angle. This incorrect geometry, leads to a quadratic phase error, and hence defocusing. We have found that a phase error of less than $\pm \pi/2$ gives an acceptable image quality. This gives the following requirement

$$|\delta z \delta h| \leq \lambda r_0 / 8. \tag{12}$$

Note that this requirement is relaxed compared to [18, page 195], and serves only as a simple rule-of-thumb for typical vehicle tracks we have experienced. The actual requirement is strongly dependent on the nature of the nonlinearity of the track itself. Rapid platform motion deviation gives more image degradation than slow motion deviation [38, chapter 5.1 and 5.4].

In the upper panel of Fig. 13, we show the vehicle depth and seafloor depth for a particular HUGIN AUV track in rough terrain. Note the large depth variations which imposes non-straight apertures. The indicated time interval 1073 s to 1127 s is a time slot for data collection for a SAS image. The lower panel shows the detrended vehicle depth where the mean and linear slope is removed for this particular data collection. We see that the track deviates 3 m from a straight line. Fig. 14 shows the SAS image from the data collected in this time interval. The image shows the wreck of the Norwegian tanker Holmengraa that was sunk during World War II in 1944.

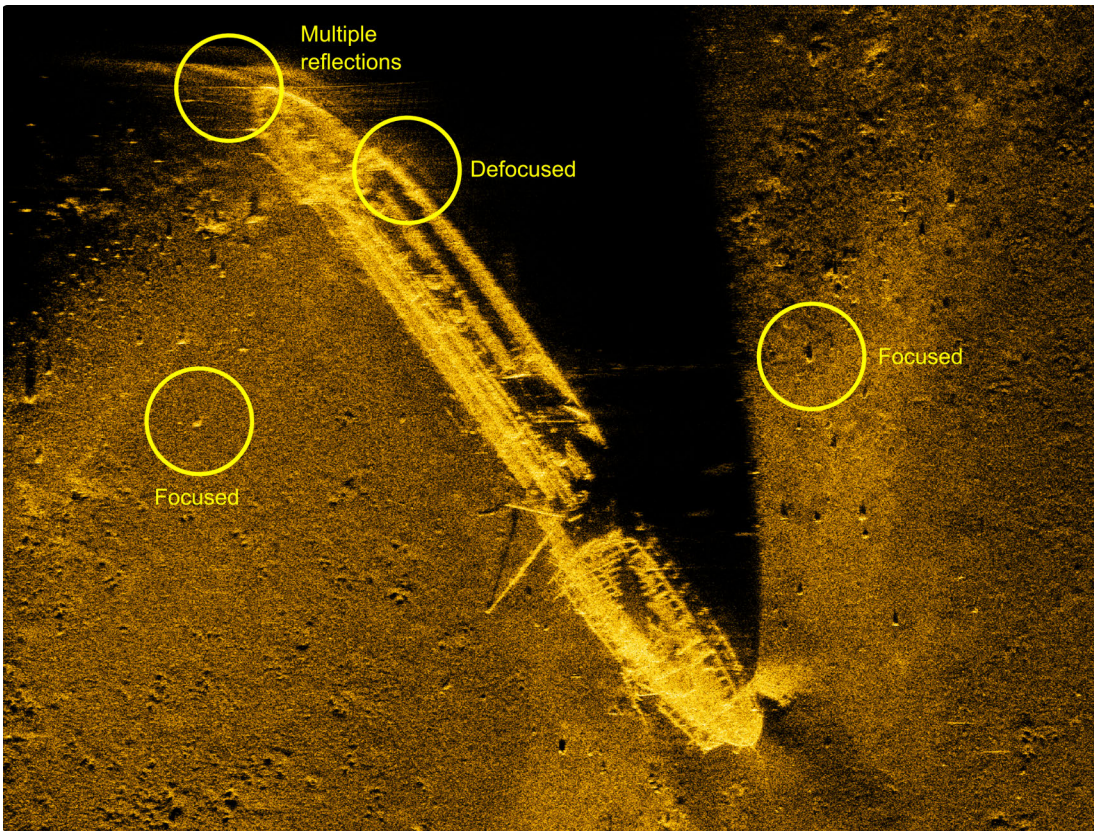Inserting $\delta z = 3$ m in (12), we get the following requirement

Fig. 14. SAS image in rough topography with motion deviations normal to the slant range direction. It shows the Norwegian tanker Holmengraa, that was sunk during WWII. The range is from $95\,\mathrm{m}$ (bottom) to $160\,\mathrm{m}$ (top) with range increasing from bottom to top.

for depth accuracy

$$|\delta h| \leq r_0 \frac{\lambda}{8} \frac{1}{\delta z} \approx 10\,\mathrm{cm} \quad \text{at } r_0 = 150\,\mathrm{m} \tag{13}$$

In Fig. 14, we see local well focused areas on the seafloor (highlighted). This indicates that the integrated navigation solution is sufficiently accurate for SAS processing. There is local defocusing, particularly visible in the bow region of the wreck. We apply real aperture interferometric mapping of the swath as part of the preprocessing before synthetic aperture imaging [29]. On a complex target such as a large wreck, there are large topographic variations and uneven backscattering strength. This is too demanding for the seafloor depth estimation algorithm, and the end bathymetric accuracy is worse than the required accuracy for this mission line. Note that the pollution in the image at far range stretching out from the bow of the wreck cannot be caused by defocusing. This is more likely caused by multiple reflections close to the bow-region of the wreck.

### D. Vehicle stability and guidance control

SAS systems are generally multi-element receiver systems. This affects synthetic aperture processing in several ways. For vehicles operated in a crabbing environment (where the heading is not aligned with the track), a baseline occurs between overlapping elements. This is illustrated in Fig. 15. Even if the track is perfectly linear, the synthetic aperture

becomes non-linear. Thus, the image quality in SAS processing becomes dependent on the topography accuracy (see the previous section). Large crab-induced baselines also makes micronavigation more challenging.

Navigation errors imposes a particular type of error in the synthetic aperture for multi-element systems. A small yaw or pitch error will cause periodic errors in the synthetic aperture, where the periodicity is constructed by the real array. This will, again, cause grating lobes in the SAS images. Fig. 16 shows an example SAS image from a HUGIN AUV mission in severe ocean currents and topography. The vehicle was crabbing with a crab angle of $18°$ during this mission. The upper panel shows the SAS image using a crab-tolerant micronavigation [44]. The lower panel shows the SAS image with default micronavigation. We see severe grating lobes in the image. The images are reconstructed using the backprojection algorithm in three dimensions. Severe crabbing also imposes restrictions on motion compensation and fast reconstruction using the wavenumber algorithm [44].
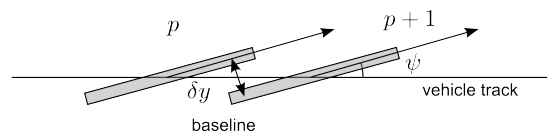


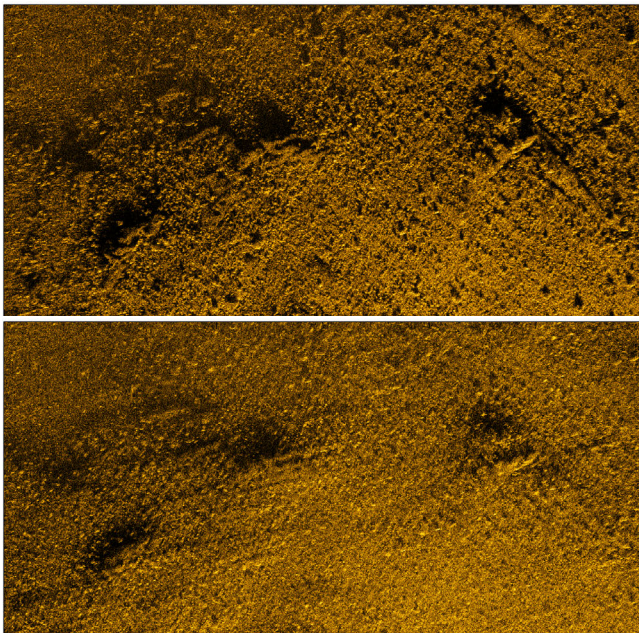Fig. 15. Multi-element receiver systems in crabbing environments.

Fig. 16. SAS image of a scene containing rocks. The range interval is 90 - 120 m (top to bottom), and the along-track size is 60 m. The images are shown with 55 dB dynamic range. Upper image: Well focused image. Lower image: Severe grating lobes caused by incorrect navigation solution. Courtesy of the Royal Norwegian Navy.

### E. Shallow waters

A fundamental challenge in high resolution imaging of the seafloor is surveying in shallow waters, where the presence of the sea surface causes interference effects which degrades the imaging quality. This applies both to real aperture sonar (or sidescan sonar [23, chapter 8.3]) and SAS. The sea surface (or seawater to air interface) is a reflector for underwater sound [22, pages 21-23], with the air-water boundary analogous to the perfect electrical conductor boundary condition from electromagnetism, e. g. all of the incident energy on the sea surface is scattered back into the ocean. The sea surface is generally random, non-stationary and rough, causing frequency dependent scattering and Doppler spread [22, chapter 9], [24, pages 122-124].

Fig. 17 shows the basic geometry for direct signals and multipath signals that have been reflected in the surface.
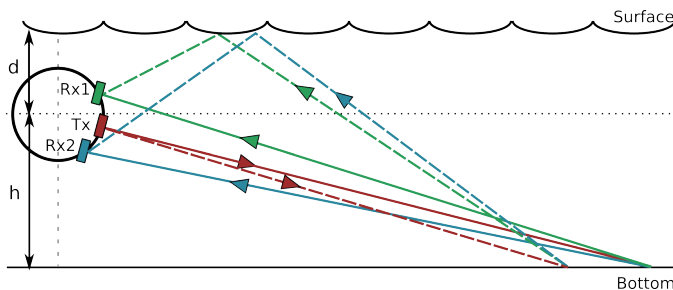


Fig. 17. Interferometric SAS in the precence of multiple reflections in shallow waters. The ray paths in the direct signal and the multipath signal has equal travel time.

Assume two receivers collecting signals $s_1$ and $s_2$ that are spatially and/or temporally displaced. We define the *complex degree of coherence* or the normalized mutual coherence function as [14, chapter 4.3]

$$\gamma_{12}(\tau) = \frac{\langle s_1(t)s_2^*(t+\tau)\rangle}{[\langle|s_1(t)|^2\rangle\langle|s_2(t)|^2\rangle]^{1/2}}, \qquad (14)$$

where $\langle\cdot\rangle$ is the expectation operator and where we have assumed local stationarity. Notice that this is identical to the normalized cross-correlation function and should not be confused with spectral coherence. The coherence as used in the radar literature [14, page 98] is usually the peak value in this function (or the zero-lag value for completely coregistered images)

$$|\gamma| = \max_\tau |\gamma_{12}(\tau)|. \qquad (15)$$

The coherence can be converted to an equivalent signal to noise ratio under certain assumptions [45], [14, chapter 4.3]

$$\text{SNR} = \frac{|\gamma|}{1-|\gamma|}. \qquad (16)$$

In shallow waters where multipath is stronger than additive noise, this can be used as a signal to multipath measurement [46]. Multipath effects are threefold:

1) The image signal-to-multipath ratio will be lower. This will cause loss of shadow contrast (or shadow depth), which again can reduce target recognition performance.
2) The spatial coherence between the upper and the lower receiver array will decrease [46]. This is due to the multiple arrival directions and different travel times caused by multipath.
3) The temporal coherence between pings (used in the principle of DPCA [27]) will be lower. This is due to the non-stationarity of the sea surface in combination with multipath.

Fig. 18 shows two SAS images of the same area of the seafloor, taken one week apart. The wind speed was relatively high during the data collection for the upper image, while during the data catch for the lower image, the sea was calm. This caused sufficient difference in sea surface roughness, which changed the multipath contribution (for a rough sea surface, less energy is scattered back into the receiver). A detailed analysis showed good agreement between the observed and modeled signal to multipath for different sea state [46]. The spatial interferometric real aperture coherence (or sidescan bathymetry coherence) for the same lines are shown in Fig. 19. Note the large difference in coherence. In the upper plot, the coherence is very high practically for full range, while in the lower plot, the coherence is high only the first third of the range. We use the spatial coherence from the real aperture interferometer for quality assessment of the data. This can, again, be used to adaptively adjust sensor settings and vehicle tracks to optimize the data quality.

### V. CONCLUSIONS

Successful generation of synthetic aperture sonar images is dependent on the ability to assess the data collection geometry and the ocean environment with sufficient accuracy. In this

paper, we have listed some of the specific challenges that have to be solved to obtain robustness and high performance. These challenges are: obtaining sufficient navigation accuracy; correcting for sound velocity errors; obtaining accurate bathymetric information; controlling vehicle motion; and operating in shallow waters in the presence of multiple reflections. Although the research on micronavigation has made a major step forward the last decade, navigation is still the most important challenge to overcome. We have described the challenges and shown example results from the HISAS interferometric SAS.

To illustrate the level of maturity reached today in interferometric SAS, we show a final example in Fig. 20. The figure shows the SAS image and the interferometric SAS relative bathymetry of a German WWII aeroplane that was found by the Royal Norwegian Navy mine warfare flotilla. These images was produced at sea by the Navy officers during the search operation.

## ACKNOWLEDGMENT

## REFERENCES

[1] L. J. Cutrona, "Comparison of sonar system performance achievable using synthetic-aperture techniques with the performance achievable by more conventional means," *J. Acoust. Soc. Am.*, vol. 58, no. 2, pp. 336–348, August 1975.

[2] M. P. Hayes and P. T. Gough, "Synthetic Aperture Sonar: A Review of Current Status," *IEEE J. Oceanic Eng.*, vol. 34, no. 3, pp. 207–224, July 2009.

[3] P. E. Hagen, N. J. Størkersen, and K. Vestgård, "HUGIN-use of UUV technology in marine applications," in *Proceedings of the OCEANS '99 MTS/IEEE*, vol. 2, Seattle, WA, USA, September 1999, pp. 967–972.

[4] H. D. Griffiths, "Synthetic aperture imaging with sonar and radar: A comparison," in *Proc. 5th World Congr. Ultrasonics*, Paris, France, 2003, pp. 511–518.

[5] P. E. Hagen, T. G. Fossum, and R. E. Hansen, "HISAS 1030: The Next Generation Mine Hunting Sonar for AUVs," in *UDT Pacific 2008 Conference Proceedings*, Sydney, Australia, November 2008.

[6] T. G. Fossum, P. E. Hagen, B. Langli, and R. E. Hansen, "HISAS 1030: High resolution synthetic aperture sonar with bathymetric capabilities," in *Shallow survey*, Portsmouth, NH, USA, October 2008.

[7] R. E. Hansen, T. O. Sæbø, H. J. Callow, P. E. Hagen, and E. Hammerstad, "Synthetic Aperture Sonar Processing for the HUGIN AUV," in *Proceedings of Oceans '05 Europe*, vol. 2, Brest, France, June 2005, pp. 1090–1094.

[8] T. O. Sæbø and B. Langli, "Comparison of EM 3000 multibeam echo sounder and HISAS 1030 interferometric synthetic aperture sonar for seafloor mapping," in *Proceedings of European Conference on Underwater Acoustic (ECUA) 2010*, Istanbul, Turkey, July 2010.

[9] R. E. Hansen, "Robust synthetic aperture sonar for autonomous underwater vehicles," in *Proceedings of Synthetic Aperture Sonar and Radar 2010*, Lerici, Italy, September 2010.

[10] M. Soumekh, *Fourier Array Imaging*. Englewood Cliffs, NJ, USA: Prentice Hall, 1994.

[11] I. G. Cumming and F. H. Wong, *Digital Processing of Synthetic Aperture Radar Data: Algorithms and Implementation*. Norwood, MA, USA: Artech House, 2005.

[12] E. C. Zaugg and D. G. Long, "Generalized Frequency-Domain SAR Processing," *IEEE Trans. Geosci. Remote Sens.*, vol. 47, no. 11, pp. 3761–3773, November 2009.

[13] H. J. Callow, "Signal Processing for Synthetic Aperture Sonar Image Enhancement," Ph.D. dissertation, University of Canterbury, Christchurch, New Zealand, 2003.
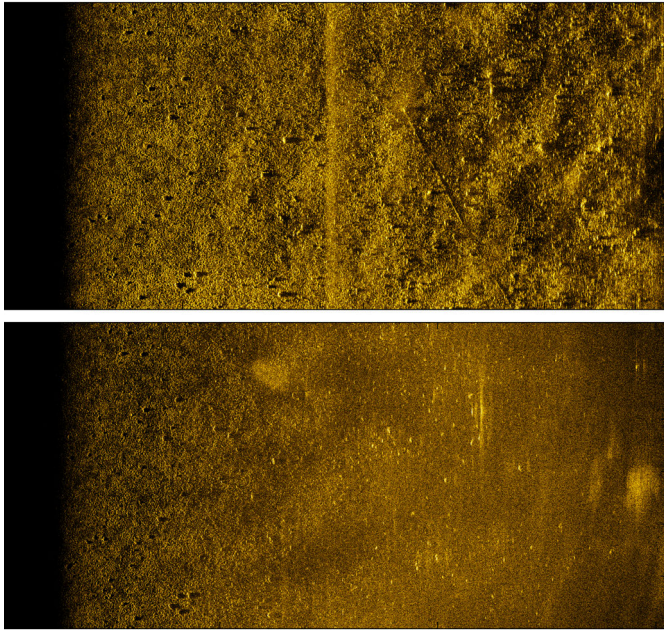
Fig. 18. The effect of multipath in shallow waters. The two images are from close to identical vehicle tracks, taken one week apart. The wind speed was relatively high during the data collection for the upper image, while during the data catch for the lower image, the sea was calm. The range interval is 0 m to 150 m (left to right), and the along-track image size is 60 m. The water depth is only 9 m, and the vehicle depth is 3 m. Notice that the line about mid-range in the upper image is an artifact caused by interference from other acoustic sensors on the AUV.
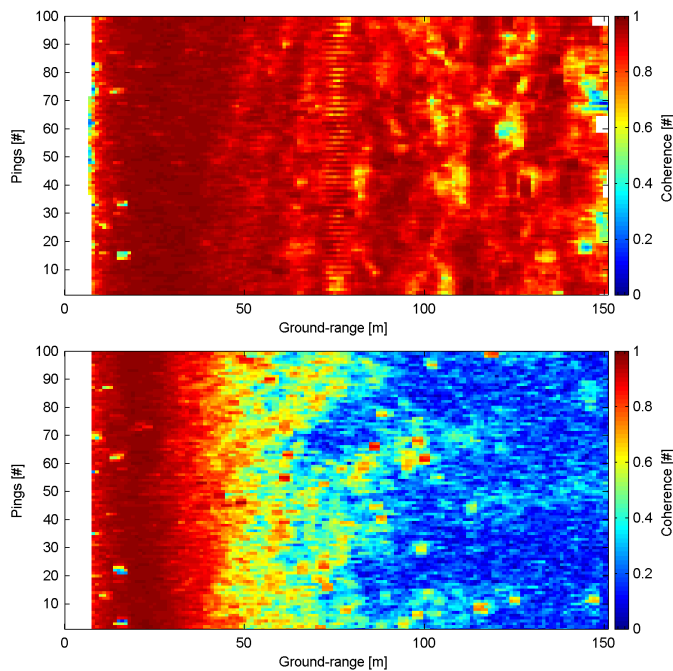


Fig. 19. Spatial coherence from real aperture interferometry from the images shown in Fig. 18. The SAS image quality is considered acceptable for coherence above 0.66 (equivalent to 3 dB SNR).
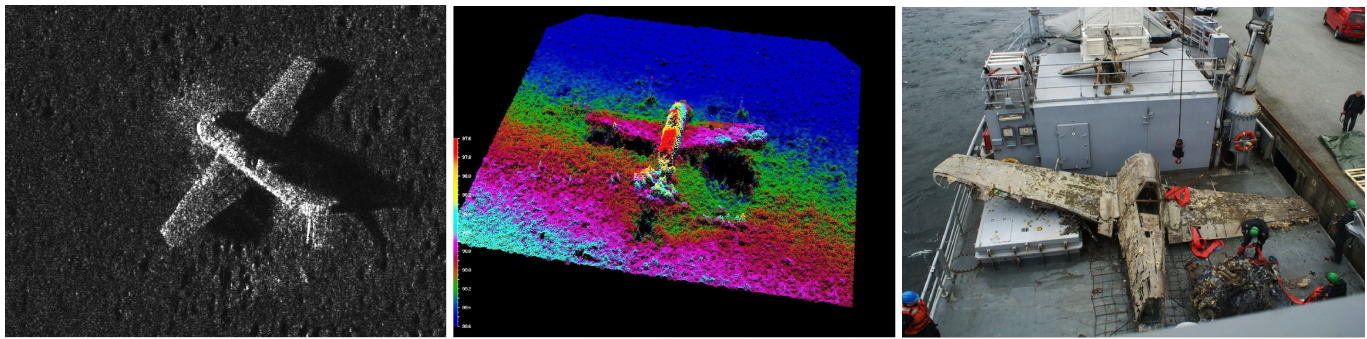
Fig. 20.   SAS image (left) and SAS bathymetry (middle) of a German WWII plane Focke Wulf 190 A-3. The range to the center of the image is 125 m The plane was found by the Royal Norwegian Navy Mine warfare flotilla at 98 m water depth during an underwater archaeology mission and measures 10.5 m between the wings. The rigth panel shows a photograph of the plane after recovery. The tail was damaged (as we see in the SAS image and the bathymetry). The motor fell off during the recovery. Courtesy of the Royal Norwegian Navy.

[14] R. F. Hanssen, *Radar Interferometry: Data Interpretation and Error Analysis*.   Dordrecht, The Netherlands: Kluwer Academic Publishers, 2001.

[15] T. O. Sæbø, B. Langli, H. J. Callow, E. O. Hammerstad, and R. E. Hansen, "Bathymetric Capabilities of the HISAS Interferometric Synthetic Aperture Sonar," in *Proceedings of Oceans 2007 MTS/IEEE*, Vancouver, Canada, October 2007.

[16] R. E. Hansen, H. J. Callow, T. O. Sæbø, P. E. Hagen, and B. Langli, "High fidelity synthetic aperture sonar products for target analysis," in *Proceedings of Oceans '08 Quebec*, Quebec, Canada, September 2008.

[17] D. H. Johnson and D. E. Dudgeon, *Array Signal Processing: Concepts and Techniques*, ser. Signal processing series.   Englewood Cliffs, NJ, USA: Prentice Hall, 1993.

[18] J. C. V. Jakowatz, D. E. Wahl, P. H. Eichel, D. C. Ghiglia, and P. A. Thompson, *Spotlight-Mode Synthetic Aperture Radar: A Signal Processing Approach*.   Dordrecht, The Netherlands: Kluwer Academic Publishers, 1996.

[19] J. Groen, R. E. Hansen, H. J. Callow, J. C. Sabel, and T. O. Sæbø, "Shadow enhancement in synthetic aperture sonar using fixed focusing," *IEEE J. Oceanic Eng.*, vol. 34, no. 3, pp. 269–284, July 2009.

[20] H. J. Callow, J. Groen, R. E. Hansen, and T. Sparr, "Shadow enhancement in SAR imagery," in *Proceedings of RADAR 2007*, Edinburgh, UK, October 2007.

[21] G. Franceschetti and R. Lanari, *Synthetic Aperture Radar Processing*. Boca Raton, FL, USA: CRC Press, 1999.

[22] L. Brekhovskikh and Y. Lysanov, *Fundamentals of Ocean Acoustics*, ser. Springer Series in Electrophysics.   Berlin, Germany: Springer-Verlag, 1982, vol. 8.

[23] X. Lurton, *An Introduction to Underwater Acoustics: Principles and Applications*.   Chichester, UK: Springer Praxis Publishing, 2002.

[24] H. Medwin and C. S. Clay, *Fundamentals of Acoustical Oceanography*. San Diego, CA, USA: Academic Press, 1998.

[25] M. P. Bruce, "A Processing Requirement and Resolution Capability Comparison of Side-Scan and Synthetic-Aperture Sonars," *IEEE J. Oceanic Eng.*, vol. 17, no. 1, pp. 106–117, January 1992.

[26] P. E. Hagen and R. E. Hansen, "Area coverage rate for Synthetic Aperture Sonars," in *Proceedings of Oceans '07 Europe*, Aberdeen, Scotland, June 2007.

[27] A. Bellettini and M. A. Pinto, "Theoretical accuracy of synthetic aperture sonar micronavigation using a displaced phase-center antenna," *IEEE J. Oceanic Eng.*, vol. 27, no. 4, pp. 780–789, October 2002.

[28] P. E. Hagen and R. E. Hansen, "Synthetic aperture sonar challenges ... and how to meet them," *Hydro International*, pp. 26–31, may 2008.

[29] R. E. Hansen, H. J. Callow, T. O. Sæbø, S. A. Synnes, P. E. Hagen, T. G. Fossum, and B. Langli, "Synthetic aperture sonar in challenging environments: Results from the HISAS 1030," in *Proceedings of Underwater Acoustic Measurements 2009*, Nafplion, Greece, June 2009.

[30] B. Jalving, K. Gade, O. K. Hagen, and K. Vestgård, "A Toolbox of Aiding Techniques for the HUGIN AUV Integrated Inertial Navigation system," in *Proceedings of Oceans 2003 MTS/IEEE*, San Diego, CA, USA, September 2003.

[31] R. E. Hansen, T. O. Sæbø, K. Gade, and S. Chapman, "Signal Processing for AUV based Interferometric Synthetic Aperture Sonar," in *Proceed-ings of Oceans 2003 MTS/IEEE*, San Diego, CA, USA, September 2003, pp. 2438–2444.

[32] C. E. Muehe and M. Labitt, "Displaced-Phase-Center Antenna Technique," *Lincoln Laboratory Journal*, vol. 12, no. 2, pp. 281–296, 2000.

[33] J. R. Fienup, "Phase error correction by shear averaging," in *Signal Recovery and synthesis III*.   Optical Society of America, 1989, pp. 134–137.

[34] K. A. Johnson, M. P. Hayes, and P. T. Gough, "A Method for Estimating the Sub-wavelength Sway of a Sonar Towfish," *IEEE J. Oceanic Eng.*, vol. 20, no. 4, pp. 258–267, October 1995.

[35] R. S. Longhurst, *Geometrical and Physical Optics*, 3rd ed.   New York, NY, USA: Longman, 1973.

[36] C. Elachi, *Spaceborne Radar Remote Sensing: Applications and Techniques*.   New York, NY, USA: IEEE Press, 1988.

[37] D. A. Cook and D. C. Brown, "Analysis of Phase Error Effects on Stripmap SAS," *IEEE J. Oceanic Eng.*, vol. 34, no. 3, pp. 250–261, July 2009.

[38] W. G. Carrara, R. S. Goodman, and R. M. Majewski, *Spotlight Synthetic Aperture Radar: Signal Processing Algorithms*.   Norwood, MA, USA: Artech House, 1995.

[39] J. H. Steele, S. A. Thorpe, and K. K. Turekian, *Encyclopedia of Ocean Sciences*, 2nd ed.   San Diego, CA, USA: Academic Press, 2009.

[40] R. E. Hansen, H. J. Callow, and T. O. Sæbø, "The effect of sound velocity variations on synthetic aperture sonar," in *Proceedings of Underwater Acoustic Measurements 2007*, Crete, Greece, June 2007.

[41] K. D. Rolt and H. Schmidt, "Effects of refraction on synthetic aperture sonar imaging," *J. Acoust. Soc. Am.*, vol. 95, no. 6, pp. 3424–3429, June 1994.

[42] J. T. Ambrose and A. Geneva, "Wide swath bathymetric sonar error modeling for a hydrographic survey ship," in *OCEANS '95 MTS/IEEE*, San Diego, CA, USA, October 1995, pp. 339–346.

[43] O. Frey, C. Magnard, M. Rüegg, and E. Meier, "Focusing of Airborne Synthetic Aperture Radar Data From Highly Nonlinear Flight Tracks," *IEEE Trans. Geosci. Remote Sens.*, vol. 47, no. 6, pp. 1844–1858, June 2009.

[44] H. J. Callow, "Comparison of SAS processing strategies for crabbing collection geometries," in *Proceedings of Oceans 2010 MTS/IEEE*, Seattle, WA, USA, September 2010.

[45] H. A. Zebker and J. Villasenor, "Decorrelation in Interferometric Radar Echoes," *IEEE Trans. Geosci. Remote Sens.*, vol. 30, no. 5, pp. 950–959, September 1992.

[46] S. A. Synnes, R. E. Hansen, and T. O. Sæbø, "Assessment of shallow water performance using interferometric sonar coherence," in *Proceedings of Underwater Acoustic Measurements 2009*, Nafplion, Greece, June 2009.

**Roy Edgar Hansen** (M'07) received the M.Sc. degree in physics in 1992, and the Ph.D. degree in physics in 1999, both from the University of Tromsø, Norway. From 1992 to 2000 he was with the Norwegian research company TRIAD, working on multistatic sonar, multistatic radar, SAR and underwater communications. Since 2000, he has been working at the Norwegian Defence Research Establishment (FFI), Kjeller, Norway. He is currently team-leader for the HUGIN autonomous underwater vehicle development and the synthetic aperture sonar development at FFI. He is also adjunct associated professor at Centre for Imaging at University in Oslo, Norway.

**Hayden John Callow** (M'07) received the BE degree in 1998 from the University of Canterbury, Christchurch, New Zealand. Since completing his Ph.D. degree on synthetic aperture sonar (SAS) image enhancement with the Acoustics Research Group, University of Canterbury in 2003, he has been working on SAS and SAR processing algorithms at the Norwegian Defence Research Establishment (FFI), Kjeller, Norway. Research interests include fast beamforming and autofocus.

**Torstein Olsmo Sæbø** (M'06) was born in Bergen, Norway, in 1977. He received the cand.scient. (M.Sc.) degree in astrophysics in 2002, from the University of Oslo, Norway. Since 2002, he has been working as a Scientist at the Norwegian Defence Research Establishment (FFI), Kjeller, Norway, specializing in the field of interferometry on synthetic aperture sonar. In 2010 he received the Ph.D degree in physics from the University of Tromsø, Norway, entitled *Seafloor Depth Estimation by means of Interferometric Synthetic Aperture Sonar*.

**Stig Asle Vaksvik Synnes** was born in Ålesund, Norway, in 1972. He received the Cand.Scient. (M.Sc.) in atomic physics from the university of Bergen, Norway, in 1997. Since 1998, he has been with the Norwegian Defence Research Establishment (FFI), Kjeller, Norway. His main research interests have been on perimeter surveillance systems, electromagnetic modeling, naval mine countermeasures and synthetic aperture sonar. SAS research include shallow water sonar performance and correlation based navigation. Currently he is working on a Ph.D in ultra wide-band SAS.